



Originally published as:

Pilz, M., Parolai, S., Woith, H. (2017 online): A 3-D algorithm based on the combined inversion of Rayleigh and Love waves for imaging and monitoring of shallow structures. - *Geophysical Journal International*, 209, 1, pp. 152—166.

DOI: <http://doi.org/10.1093/gji/ggx005>

# A 3-D algorithm based on the combined inversion of Rayleigh and Love waves for imaging and monitoring of shallow structures

Marco Pilz,<sup>\*</sup> Stefano Parolai and Heiko Woith

GFZ German Research Center for Geosciences, Helmholtzstr. 7, D-14467 Potsdam, Germany. E-mail: [pilz@gfz-potsdam.de](mailto:pilz@gfz-potsdam.de)

Accepted 2017 January 5. Received 2017 January 4; in original form 2016 June 5

## SUMMARY

In recent years, there has been increasing interest in the study of seismic noise interferometry as it can provide a complementary approach to active source or earthquake-based methods for imaging and continuous monitoring the shallow structure of the Earth. This meaningful information is extracted from wavefields propagating between those receiver positions at which seismic noise was recorded. Until recently, noise-based imaging relied mostly on Rayleigh waves. However, considering similar wavelengths, a combined use of Rayleigh and Love wave tomography can succeed in retrieving velocity heterogeneities at depth due to their different sensitivity kernels. Here, we present a novel one-step algorithm for simultaneously inverting Rayleigh and Love wave dispersion data aiming at identifying and describing complex 3-D velocity structures. The algorithm may help to accurately and efficiently map the shear wave velocities and the Poisson ratio of the surficial soil layers. In the high-frequency range, the scattered part of the correlation functions stabilizes sufficiently fast to provide a reliable estimate of the velocity structure not only for imaging purposes but also allows for changes in the medium properties to be monitored. Such monitoring can be achieved with a high spatial resolution in 3-D and with a time resolution as small as a few hours. In this paper, we describe a recent array experiment in a volcanic environment in Solfatara (Italy) and we show that this novel approach has identified strong velocity variations at the interface between liquids and gas-dominated reservoirs, allowing localizing a region which is highly dynamic due to the interaction between the deep convection and its surroundings.

**Key words:** Surface waves and free oscillations; Seismic tomography.

## 1 INTRODUCTION

It has long been known that it is possible to study Earth's structure using the seismic noise wavefield. In his pioneering work, based on primary findings by Akamatsu (1956a,b) on the origin and the correlation of seismic noise, Aki (1957) noted that the seismic wavefield from different noise sources shows a spatial coherence. He suggested that observing such spatial correlation could provide an accurate way of measuring the wavelength of surface waves at distinct frequencies, and, therefore, through an inversion of the dispersion curve, could give the structure of the subsurface at a given site. Later on, Claerbout (1968) stressed that this observation could be extended for distances much larger than the wavelength. He conjectured that the spatial correlation of seismic waves, averaged over time, should yield the actual impulse response of the medium. This

property was demonstrated theoretically in a 1-D layered medium (Claerbout 1968). However, it was not generalized to 3-D media at that time and it was further found to have only feeble experimental confirmations.

More recently, Weaver & Lobkis (2001) demonstrated that the time-averaged correlation of diffuse ultrasound or ultrasonic noise yields the elastic Green's function of the medium, forming the basis for applications in seismology (Campillo & Paul 2003; Shapiro & Campillo 2004). Nowadays, seismic noise tomography has been widely used on regional and continental scales to infer Rayleigh (Shapiro *et al.* 2005; Yao *et al.* 2006; Yang *et al.* 2007) and Love wave (Cho *et al.* 2007; Lin *et al.* 2008) group and phase speeds and to study the shallow structure of the Earth. In most applications, strong surface wave signals within the microseism frequency band (0.05–0.2 Hz) are extracted followed by traditional surface wave tomography methods for inverting for 3-D shear velocity structures (e.g. Yao *et al.* 2008; Moschetti *et al.* 2010).

For studying local structures, the same principle can also be applied on much smaller scales. In particular, on such scales the reliable determination of the elastic properties of near-surface

<sup>\*</sup>Now at: Swiss Seismological Service, Swiss Federal Institute of Technology, Sonneggstr. 5, 8092 Zurich, Switzerland. E-mail: [marco.pilz@sed.ethz.ch](mailto:marco.pilz@sed.ethz.ch)

materials and their influence on seismic wave propagation are of fundamental interest in ground water, engineering, reservoir monitoring and environmental studies. In the past, such noise-based techniques have been applied to a small-scale array in Spain (Chávez-García & Luzón 2005) as well as for imaging volcanic edifices (Brenquier *et al.* 2007; Nakata *et al.* 2016), shallow impedance contrasts (Picozzi *et al.* 2009), oil fields (de Ridder & Dellinger 2011; Mordret *et al.* 2013), landslides (Renalier *et al.* 2010; Pilz *et al.* 2014) and the surface traces of seismic faults (Pilz *et al.* 2013) with the latter works not only mapping surface wave velocities but directly accounting for the 3-D *S*-wave velocity structure.

So far, there is only limited effort in the near-surface community on utilizing Love waves compared to Rayleigh waves because of the higher locally generated noise on the horizontal components and general belief that the seismic noise sources would be ineffective at directly generating Love waves due to total internal, multiple reflections of *SH* waves (Bullen & Bolt 1985). However, Métaxian *et al.* (1997), Tokimatsu (1997), Chouet *et al.* (1998) and Saccorotti *et al.* (2003) found evidences for a dominance of Love waves in high-frequency seismic noise data and signals of volcanic tremor. Therefore, the complementary information of Rayleigh and Love waves can allow a simultaneous inversion of their phase velocities to study the shallow structure of the Earth (Lee & Solomon 1979; Köhler *et al.* 2007), thereby reducing the degree of non-uniqueness of an inverted *S*-wave velocity model (Boxberger *et al.* 2011).

The distribution of noise sources strongly controls the quality of the Green's function. Most of the seismic noise sources are superficial and result from the interaction between the oceans, the atmosphere or the human activities with the solid Earth. As a consequence, the fundamental mode of surface waves can be extracted more easily from noise correlations (Kimman & Trampert 2010). However, if the noise sources are not distributed isotropically, this may result in preferential reconstruction and reduced convergence of the Green's function (e.g. Snieder 2004; Stehly *et al.* 2006). The length of the seismic noise record required to converge to a stable correlation function is controlled by the nature of the noise, the distance between sensors and by the intrinsic attenuation and scattering properties of the studied medium. At frequencies higher than a few Hertz, the coherence buildup in a correlation function is of the order of a few hours (Sabra *et al.* 2005; Brenquier *et al.* 2007; Larose *et al.* 2008), meaning that such imaging methods can be repeated in this time frame. In volcanic environments, such monitoring methods can provide useful insights into the dynamics of magma pressurization and transport. Pressurized volcanic fluids (magma and water) or gas induce deformation and thus perturbations of the elastic properties of volcanic edifices. In turn, such small perturbations can be detected as changes of seismic wave properties based on seismic noise (e.g. Ratomopurbo & Poupinet 1995; Miller & Smith 1999; Grêt *et al.* 2005; Wegler *et al.* 2006). However, despite considerable efforts in the past, the precise monitoring of the location of subsurface changes has proven to be difficult, meaning that there is a need for novel observational methods to obtain information about the ongoing subsurface changes and their relation to volcanic processes.

In this paper, we will demonstrate that continuous recordings of high-frequency seismic noise can effectively be used not only for 3-D *S*-wave tomography but they further allow constraining the *P*-wave velocity structure. This novel inversion approach is applied to seismic noise recorded by a 2-D seismic array at the Solfatara crater (Italy), where independent geological and geophysical information is available. We will present quality measures from noise

spectral analysis. We will introduce the methodology for combining Rayleigh and Love waves followed by a numerical verification. Finally, we will present a temporarily and spatially resolved 3-D image of the Solfatara crater.

## 2 DATA PROCESSING

Several approaches have been proposed in the literature to extract information about the velocity of seismic wave propagation in the shallow structure from seismic noise recordings. In general, all methods for retrieving surface wave dispersion curves are based on phase-coherence measurements between pairs (at least two) of signals. To extract surface wave dispersion curves, Aki (1957) proposed the spatial autocorrelation (SPAC) method, which has been generalized to the extended spatial autocorrelation method by Ohori *et al.* (2002). Further methods use different transforms and they obtain similar results, for example, the slant-slack transform (McMechan & Yedlin 1981), the frequency–wavenumber analysis (maximum likelihood method, Capon *et al.* 1967; Capon 1969; Horike 1985) and the multichannel analysis of surface waves (Miller *et al.* 1999; Park *et al.* 1999).

As discussed in Ohori *et al.* (2002), if the microtremor wavefield is stochastic and stationary in both space and time, the azimuthally averaged correlation function for one angular frequency  $\omega_0$  can be expressed in the form

$$\rho(r, \omega_0) = J_0 \left( \frac{\omega_0}{c(\omega_0)} r \right), \quad (1)$$

where  $c(\omega_0)$  is the phase velocity,  $r$  is the interstation distance and  $J_0$  is the zero-order Bessel function. Eq. (1) can be applied to averaged correlation functions calculated for a set of narrow frequency bands. In this study, however, we apply an alternative frequency-domain formulation of the method that is complementary to the zero-crossing method (Ekström *et al.* 2009). The method has been shown to be insensitive to the power spectrum of the background noise and the non-linear filtering of the original signal. It further provides similar results for high signal-to-noise ratios (SNR), but substantially improves for lower SNRs (Ohori *et al.* 2002; Okada 2003; Menke and Jin 2015).

From the correlation theorem (e.g. Bracewell 1983), the spatial correlation value for a given station pair in the frequency domain  $\rho(\omega_0)$  can be written as (Malagnini *et al.* 1993; Métaxian *et al.* 1997)

$$\rho(\omega_0) = \frac{\frac{1}{M} \sum_{l=1}^M \text{Re} ({}_m S_{jn}(\omega_0))}{\sqrt{\frac{1}{M^2} \sum_{m=1}^M {}_m S_{jj}(\omega_0) \sum_{m=1}^M {}_m S_{nn}(\omega_0)}}. \quad (2)$$

Herein,  ${}_m S_{jn}$  describes the cross-spectrum of the  $m$ th segment between the  $j$ th and the  $n$ th station of the array. The power spectrum of the segment  $m$  at station  $j$  and  $n$  is given by the terms  ${}_m S_{jj}$  and  ${}_m S_{nn}$ , respectively. The symbol  $\text{Re}(\dots)$  indicates the real part of the complex quantity in brackets.

Eq. (2) combines two strategies, namely averaging and normalization, to enhance the estimation of the correlation function. We use Bartlett's method (Bartlett 1948) to reduce the variance of the periodograms and to improve the statistical properties of both functions. Eq. (2) is used to compute  $\rho(\omega_0)$ , that is, the azimuthal average of the correlation function (Henstridge 1979).

Although nowadays they are mainly used for the vertical component only, Aki (1965) showed that the SPAC equations derived for the analysis of the vertical component of ground motion can in

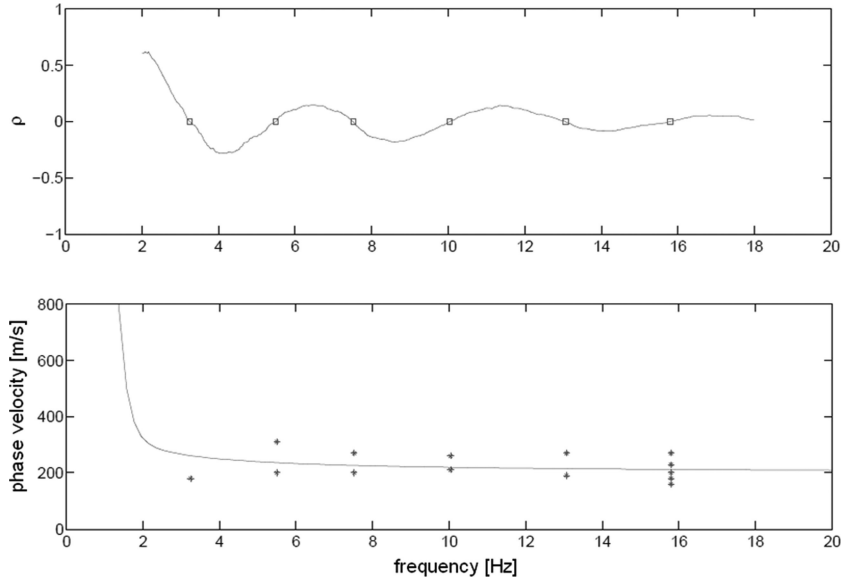


**Figure 1.** Top: example of the correlation function (grey line) between two stations at a distance of 49 m with zero crossings indicated (squares). Bottom: corresponding phase velocity dispersion curve (grey line) according to eq. (4) estimated by least-squares fit to possible velocities estimated from the zero crossings (black dots).

principle be adapted also for the analysis of the horizontal components, with the aim of extracting the phase velocities of Rayleigh and Love waves. In fact, if Rayleigh waves are polarized parallel to the propagation direction, equations similar to eq. (1) can be derived for both the radial and tangential components of motion, and similarly for Love waves when they are perpendicularly polarized to the direction of propagation.

However, during real surveys, seismic noise in the horizontal components of ground motion will be characterized by a superposition of both Rayleigh and Love waves. Thus, the extraction of phase-velocity information for the single phases is not straightforward. For this reason, Métaxian *et al.* (1997) proposed, under the assumption that the contributions of both Rayleigh and Love waves are statistically independent, to adopt the equations

$$\begin{aligned} \rho_r(r, \omega_0) &= \alpha \left[ J_0 \left( \frac{\omega_0 r}{c_R(\omega_0)} \right) - J_2 \left( \frac{\omega_0 r}{c_R(\omega_0)} \right) \right] \\ &\quad + (1 - \alpha) \left[ J_0 \left( \frac{\omega_0 r}{c_L(\omega_0)} \right) + J_2 \left( \frac{\omega_0 r}{c_L(\omega_0)} \right) \right] \\ \rho_t(r, \omega_0) &= \alpha \left[ J_0 \left( \frac{\omega_0 r}{c_R(\omega_0)} \right) + J_2 \left( \frac{\omega_0 r}{c_R(\omega_0)} \right) \right] \\ &\quad + (1 - \alpha) \left[ J_0 \left( \frac{\omega_0 r}{c_L(\omega_0)} \right) - J_2 \left( \frac{\omega_0 r}{c_L(\omega_0)} \right) \right] \end{aligned} \quad (3)$$

where  $\alpha(\omega)$  represents the proportion of Rayleigh and Love waves in the wavefield energy.  $J_2$  is the second-order Bessel function. In particular, for  $\alpha = 1$ , the wavefield is fully composed of Rayleigh waves, while for  $\alpha = 0$ , only Love waves exist. Eq. (3) can therefore be exploited to retrieve Love wave phase velocity estimates and information on the relative fraction of Rayleigh and Love waves. Once the Rayleigh wave phase velocities are constrained by the analysis of the vertical component of motion (using, e.g. a grid search procedure, see Parolai *et al.* 2006), a similar iterative procedure can be implemented for the horizontal components of motion for the estimation of Love wave phase velocities, with the only addition of a loop accounting for the variation of the parameter  $\alpha$ .

For calculating the surface wave velocities between the stations, the continuous recordings were divided into segments of two hours. This time frame has been found to be the shortest fraction of time providing stable correlation functions (Larose *et al.* 2008). After removing the instrumental response, a time-domain running absolute-mean normalization was applied to eliminate the effect of large transient signals (Bensen *et al.* 2007) when calculating the cross spectra. For each of the  $N(N-1)/2$  possible station pairs, where  $N$  is the number of stations, the individual traveltimes between the stations were calculated based on the weighted velocity values at the zero crossings of the Bessel function using the known distances between the sensors.

The key part of the procedure is the use of a grid search algorithm based on eq. (1) to find the best fit to the correlation values. We first smooth the correlation values in eq. (1) using a running average to reduce the possibility of noise causing several extremely closely spaced zero crossings. For each interstation pair, a velocity range from 50 to 1000 m s<sup>-1</sup> is scanned sequentially in steps of 10 m s<sup>-1</sup>, searching for adjacent elements of opposite sign, and using linear interpolation to estimate the frequency at which the zero crossing occurs (Fig. 1). Moreover, the double of the minimum velocity from all zero crossings is used to filter out outliers. Of course, for different interstation pairs the zero crossings will occur at different frequencies.

As the phase velocities of surface waves generally lie within a narrow range of plausible values and, moreover, as they tend to vary smoothly with frequency, reflecting the way in which the waves average the shallow structure, a typical phase velocity curve can be approximated by its values at just a few frequencies, with other values filled in by interpolation. As for the inversion procedure, the phase velocity value for a single given frequency has to be known for all interstation pairs, a custom exponential curve fit according to Tang *et al.* (2010) is then applied by

$$c(\omega_0) = m \tanh^{-1}(n\omega_0) + q/\sqrt{\omega_0}. \quad (4)$$

The variables  $m$ ,  $n$  and  $q$  are used to constrain the phase velocity values  $c(\omega_0)$  to physically reasonable ranges for given values of

$\omega_0$  spread over the frequency range of interest. Please note that the fitting curve function as given by eq. (4) is not unique. Other functional forms, as long as they mimic the global trend of the dispersion characteristics, can be used.

### 3 THE INVERSION ALGORITHM

One important development in methodology sets this work apart from previous studies: Usually, 3-D velocity models are obtained by interpolation between individual 1-D velocity profiles from inverted group or phase velocity dispersion curves. In our study, we go one step further by inverting the estimated surface wave traveltimes between the sensors of the array chosen for each frequency by a rapid tomographic algorithm. We decided in favour of this approach to calculate a 3-D velocity model instantaneously, keeping in mind an application for monitoring changes in the medium properties.

All data processing described hereafter begins with the Rayleigh and Love wave traveltimes for each station pair from the vertical-vertical (ZZ) and transverse-transverse (TT) cross-correlations. As will be shown in the following, the Green's function has the same form, meaning that the same phase velocity analysis can be applied to both Rayleigh and Love waves.

The individual traveltimes between all stations were inverted by a tomographic approach to calculate 3-D Rayleigh and Love velocity models. In a general form, the traveltime  $t$  between two receivers along a ray path  $L$  along a line element  $dl$  for a continuous slowness  $s$  (inverse velocity) is given in an integral form

$$t = \int_L s dl. \quad (5)$$

Although the ray path is velocity dependent, meaning that travel-time inversion is a non-linear problem, deviations of the paths from a straight line will either be of the same order as the dimension of the blocks or will be less than a quarter of the wavelength (Long 2000). On the one hand, deviations smaller than the block size will not introduce significant errors and, on the other, deviations smaller than a quarter wavelength are within the limits of image resolution. On the global scale, Rawlinson & Spakman (2016) showed that even when significant anomalies (up to 20 per cent) are present and even in regions with good angular path coverage, the non-linear propagation error is much smaller relative to the amplitude of the reproduced anomalies. Hence, keeping in mind that there is also a small level of error for the input data for shallow seismic surveys and the scale-invariance expected from theoretical considerations, we are sure that a bias of a few percent can be tolerated to keep the solution linear. Consequently, the entire medium of interest can be subdivided into a number of smaller cells, meaning that the problem can be expressed in a simple discrete matrix form to be used in practical applications

$$\mathbf{t}_i = \mathbf{L}_i \mathbf{s}_i, \quad (6)$$

in which  $i$  represents Rayleigh and Love waves, respectively.  $\mathbf{L}$  is an  $RF \times MH$  matrix with  $R$  being the number of rays for  $F$  different frequencies crossing the studied medium that is subdivided into  $M$  cells in each of the  $H$  horizontal layers (for details see Pilz *et al.* 2012, 2013). Obviously, such kind of pre-conditioning (i.e. the number and the size of the cells) favours the control over size and amplitude of the structure that is recovered. However, we decided for a uniformly distributed regularization without accounting for variations in the information content of the data. For a frequency range higher than a few Hertz and corresponding low-velocity surficial soil layers, a cell size of several metres will provide balanced ray coverage in each

cell. The vector  $\mathbf{t}$  in eq. (6) corresponds to the traveltimes between each pair of receivers with a frequency-dependent slowness  $\mathbf{s}$ . The phase velocity is assumed to be constant within each of the cells and, therefore, the propagation paths can be considered to be straight rays within the cells.

In general, uncertainties in measured traveltimes between two sensors can degrade the solution and can produce spurious velocity anomalies. We adopted an iterative procedure for solving eq. (6) using damped least squares or singular value decomposition, following Long & Kocaoglu (2001). Starting from a homogeneous 3-D velocity model, an iterative procedure using singular value decomposition for minimizing the misfit between the observed and theoretical traveltimes is adopted. We further constrain the solution by making use of a damping coefficient  $\varepsilon$ . As pointed out by Marquardt (1963), the damping factor significantly controls the speed of convergence and further acts as a constraint on the model space (Tarantola 1987). Since shallow blocks are sampled much stronger by higher frequencies and since the deeper ones are sampled only by lower frequencies, we introduce a further constraint on the solution by adding a  $MHF \times MHF$  weighting matrix. According to Yanovskaya & Ditmar (1990), for a 3-D problem, the weights turn out to be representable as a product of two functions, one depending on the horizontal properties, that is, the number, path length in consideration of the relief and orientation of the ray paths and the other one depending on the depth, that is, the frequency. For the horizontal coordinates, the singular values ( $a_1, a_2$ ) of the ray density matrix were used to calculate its ellipticity  $\sqrt{(a_1^2 - a_2^2)/a_1^2}$ , based on a proposal of Kissling (1988). If many different rays with different azimuths cross the cell, the ellipticity is close to 1 and a good resolution is achieved. Therefore, the horizontal weights were computed by multiplying the ellipticity for the number of rays crossing each cell. On the other hand, the vertical weights account for the different penetration depths of the different frequencies for Rayleigh and Love waves separately. The vertical weights are based on the analytical solution of displacement components in a half-space for the fundamental mode of Rayleigh waves (Aki & Richards 1980) and Love waves (Borcherdt 2008) taking into account the different penetration depths of the individual frequencies (Fig. 2). For Love waves, we obtain

$$u(|\mathbf{z}|) = \cos(\text{Re}[B_n] \mathbf{z} \cdot \mathbf{e}_z) e^{i \frac{\omega_0}{c_{\text{Love}(\omega_0)}} \mathbf{z} \cdot \mathbf{e}_z}, \quad (7)$$

where  $\mathbf{z} \cdot \mathbf{e}_z = |\mathbf{z}| \cos(\alpha)$  is the scalar product of  $\mathbf{z}$ , measured perpendicular to the surface of the cell, and the unit vector  $\mathbf{e}_z$ , where  $\alpha$  is the slope of surface topography for each of the cell columns. For the entire surface of the block, we define  $|\mathbf{z}| := 0$ , that is, we set the elevation to zero. Please note that the scheme can account for different values for  $\alpha$  for different parts of the block. In eq. (7), the principal value  $B_n$  is defined by  $B_n := \sqrt{k_{h \text{ Love}} - k_S}$  (Borcherdt 2008).  $k_{h \text{ Love}} = \omega_0 / c_{h \text{ Love}}(\omega_0)$  is the Love wave number in the  $h$ th layer with  $c_{h \text{ Love}}(\omega_0)$  being the Love wave phase velocity and  $\omega_0$  being the angular frequency. Likewise,  $k_S = \omega_0 / v_S$  with  $v_S$  being the S-wave velocity.

The corresponding vertical weights  $w$  for the different frequencies are calculated as the normalized average values of  $u$  for each cell,

$$w = \frac{\int_{r_1}^{r_2} u(z) dz}{\int_0^\infty u(z) dz} \quad (8)$$

with  $r_1$  and  $r_2$  being the bounds at which  $u$  is crossing the cell limits, respectively (see Fig. 2). If no rays are crossing the cell, the weight is equal to zero. Since eqs (7) and (8) strongly depend

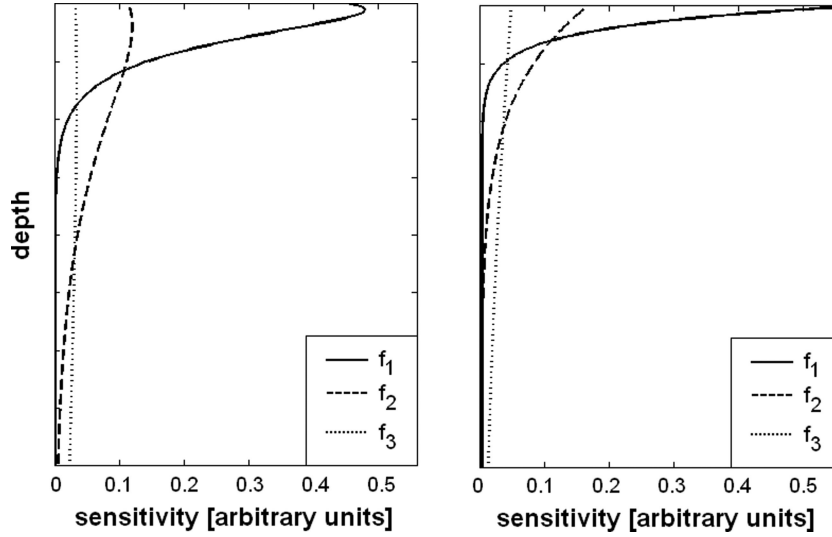


**Figure 2.** Normalized depth sensitivity kernels for Rayleigh (left) and Love (right) waves at a selection of frequencies ( $f_1 > f_2 > f_3$ ).

on the underlying phase velocities, the weights for all cells, and accordingly the velocity vectors, are updated after each iteration step.

Since Love waves are independent of the  $P$ -wave velocity, they alone can be used to obtain models of the  $S$ -wave velocity. Therefore, the final 3-D  $S$ -wave velocity model is retrieved recursively from the updated Love wave phase velocity by means of non-trivial plane-wave solution (Borcherdt 2008)

$$\mathbf{F}_{n-1} = \frac{-\mathbf{F}_{n-1}}{M_n B_n}, \quad (9)$$

where  $\mathbf{F}_{n-1} = \mathbf{f}_{n-1} \mathbf{f}_{n-2} \mathbf{f}_{n-3} \dots \mathbf{f}_1$  and

$$\mathbf{f}_m = \begin{pmatrix} \cos[-i B_m d_m] & \frac{\sin[-i B_m d_m]}{-i M_m B_m} \\ i M_m B_m \sin[-i B_m d_m] & \cos[-i B_m d_m] \end{pmatrix} \quad (10)$$

with  $M_m = \rho_m v_{S m}$  and  $d_m = i B_m$ .

For Rayleigh waves, the vertical displacements can be calculated through

$$u(|z|) = l e^{i k_{\text{Rayl}} z} e_z - s e^{p k_{\text{Rayl}} z} e_z \quad (11)$$

with  $k_{\text{Rayl}} = \omega_0 / 1 c_{\text{Rayl}} (\omega_0)$  being the Rayleigh wave number. For the starting model, we fix the parameters in eq. (11) to  $l = 0.8475$ ,  $p = 0.3933$  and  $s = 1.4679$  (Bullen 1963; Lay & Wallace 1995). Correspondingly, we are able to calculate a 3-D model of the Poisson ratio  $\nu$  for each cell through

$$\nu = \frac{Q - 0.5}{Q - 1} \quad (12)$$

with

$$Q = \frac{16 - 24 \left( \frac{c_{\text{Rayl}}}{v_s} \right)^2 + 8 \left( \frac{c_{\text{Rayl}}}{v_s} \right)^4 - \left( \frac{c_{\text{Rayl}}}{v_s} \right)^6}{16 - 16 \left( \frac{c_{\text{Rayl}}}{v_s} \right)^2}. \quad (13)$$

The 3-D model of  $v_s$  is obtained from eq. (9) and  $c_{\text{Rayl}}$  from the inversion of the ZZ cross-correlations using a singular value decomposition technique (e.g. Golub & Reinsch 1970; Arai & Tokimatsu 2004; see Pilz *et al.* 2012 for details.).

The  $P$ -wave velocity for each cell is given by

$$v_p = \sqrt{\frac{2 - 2\nu}{1 - 2\nu}} v_s. \quad (14)$$

For each iteration, the parameters in eq. (11) for every cell are updated by means of

$$l = \sqrt{\left( \frac{c_{\text{Rayl}}}{v_p} \right)^2 - 1},$$

$$p = \sqrt{\left( \frac{c_{\text{Rayl}}}{v_s} \right)^2 - 1}, \quad (15)$$

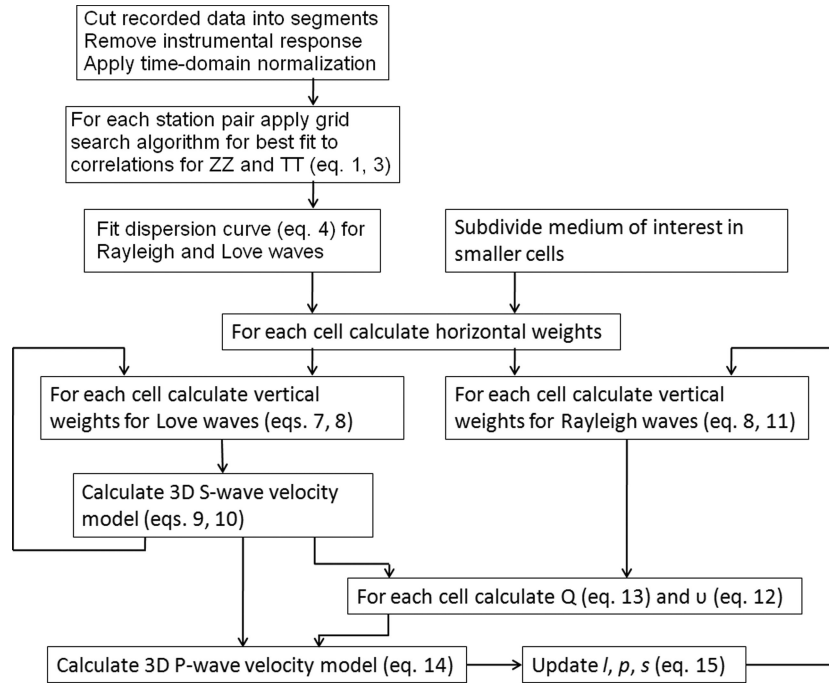
$$s = \frac{2 - \left( \frac{c_{\text{Rayl}}}{v_s} \right)^2}{2 \sqrt{\left( \frac{c_{\text{Rayl}}}{v_s} \right)^2 - 1}}.$$

Fig. 3 represents an overview of the individual steps carried out for the construction of the  $P$ - and  $S$ -wave velocity models.

Additionally, to reduce the risk of divergence and to stabilize the iteration process, an adaptive bi-weight estimate is applied (Tukey 1974; Arai & Tokimatsu 2004). Such type of maximum likelihood estimate constrains the solution to vary rather smoothly in the horizontal domain, that is, the slowness of each cell is related also to the slowness of all the surrounding cells. The functional form of the vertical weighting scheme (eqs 7 and 11) induces that the slowness also varies smoothly vertically. The weights for all cells, and accordingly the velocity vectors, are updated for each iteration step until a reasonable compromise between the reduction of the rms error between the observations and the predictions and the norm of the solution is reached.

#### 4 THE SOLFATARA CRATER: CHARACTERISTICS AND DATA ACQUISITION

The analysed natural example for obtaining temporarily resolved images by means of real-world data is a shallow volcanic crater in the Phlegrean Fields volcanic complex at Pozzuoli, near Naples, Italy, where a significant level of volcanic-hydrothermal activity is presently concentrated (Fig. 4). The Phlegrean Fields is a nested and resurgent caldera with recent volcanic activity, the last of which was the 1538 Monte Nuovo eruption. Recently, the area has seen three



**Figure 3.** A schematic description of the calculation of the  $P$ - and  $S$ -wave velocity models.

unrest episodes, in 1970–1972, in 1982–1984 and in 2010–2012, which were characterized by large ground deformation, changes in geochemical signals at the surface and some limited seismicity (e.g. Madonia *et al.* 2008). As part of the Phlegrean Fields, the Solfatara crater is a  $0.4 \times 0.5$  km subrectangular structure whose geometry is mainly due to the control exerted by N40–50W and N50E trending normal fault systems (Petrosino *et al.* 2012), along which geothermal fluids can ascend. These systems crosscut the study area and have been active several times in the past. The geophysical structure below the Solfatara area has been investigated on various spatial scales using different geophysical methods like gravity, electric resistivity and thermal imaging (Petrosino *et al.* 2006, 2012; Bruno *et al.* 2007; Letort *et al.* 2012; Byrdina *et al.* 2014; Vilardo *et al.* 2015). Recently, Serra *et al.* (2016) investigated the shallow structure of a small part of the Solfatara crater using active seismic methods but their penetration depth was limited to 15 m.

Electromagnetic and electrical data could distinguish two main zones, an outcropping resistive layer composed of non-saturated clays overlying a conductive layer corresponding to a hydrothermal aquifer. At a deeper level, the existence of a gas and/or fluid reservoir has been confirmed through recent seismic attenuation imaging (De Siena *et al.* 2010) which could recognize a vertically extending and high-attenuating structure. Although diffuse soil degassing occurs throughout the entire area of the Solfatara crater (Chiodini *et al.* 2011), fumarolic activity is mainly concentrated in its eastern part (so-called Bocca Grande, see Fig. 4) at the intersection of the N50W and N50E trending fractures that border the northeastern and southeastern part of the crater. The central part of the Solfatara crater is occupied by the Fangaia mud pool, at which the water table emerges and a continuous rising of hydrothermal fluids generates intense bubbling. Soil temperature distribution (Chiodini *et al.* 2011) also shows direct control exerted by the structures on the heat flux, as demonstrated by the alignment of the highest temperature measures along the direction of the main fracture systems, in the northeastern and southeastern parts of the crater, as well as in the Fangaia area (Granieri *et al.* 2010). On the contrary, the northwest-

ern part of the crater is relatively inactive with respect to heat flux and fumarolic activity.

Here, we study temporal and spatial variations in the velocity structures below Solfatara. The area comprises very different kinds of soils, from soft areas around the mud pools in the centre, to the dry and solid clays in the southern parts. Between 2014 May 19 and 22 and November 9 and 12, 50 seismic sensors were deployed irregularly on the surface of the crater, covering an area of  $350 \text{ m} \times 320 \text{ m}$  (see Fig. 4). Each 24-bit digitizer was synchronized using GPS reference time and recorded seismic noise continuously on more than three consecutive days at 400 samples per second. The relative position of the arrays nodes was determined with a theodolite to an accuracy of several centimetres. Every sensing unit was connected to an external, PE-6/B 3-component, 4.5 Hz geophone providing an excellent SNR on all three components for frequencies higher than 1 Hz (Strollo *et al.* 2008).

The continuous data sets were divided into fractions of two hours, resulting in 37 blocks for the May and in 39 blocks for the November campaigns. Subsequently, each block was divided into 240 windows of 30 s. After applying a second-order Butterworth high-pass filter using a corner frequency of 0.9 Hz, the corresponding dispersion curves and traveltimes between all stations have been calculated.

When calculating the path length between the individual stations we did not take into account the topographic relief as the maximum difference in altitude is of the order of a few metres only over a horizontal distance of some hundred metres. The entire inversion algorithm is repeated continuously for each data block which allows a temporarily resolved imaging of the subsurface as well as continuous data quality measurements from the noise spectral analysis.

## 5 SEISMIC DATA QUALITY CHECK

For an overview of the data stability, we calculated power spectral density (PSD) probability density functions (McNamara & Buland 2004). For each fraction of two hours, we processed time-series 900 s long, from which we removed the mean. Each time-series

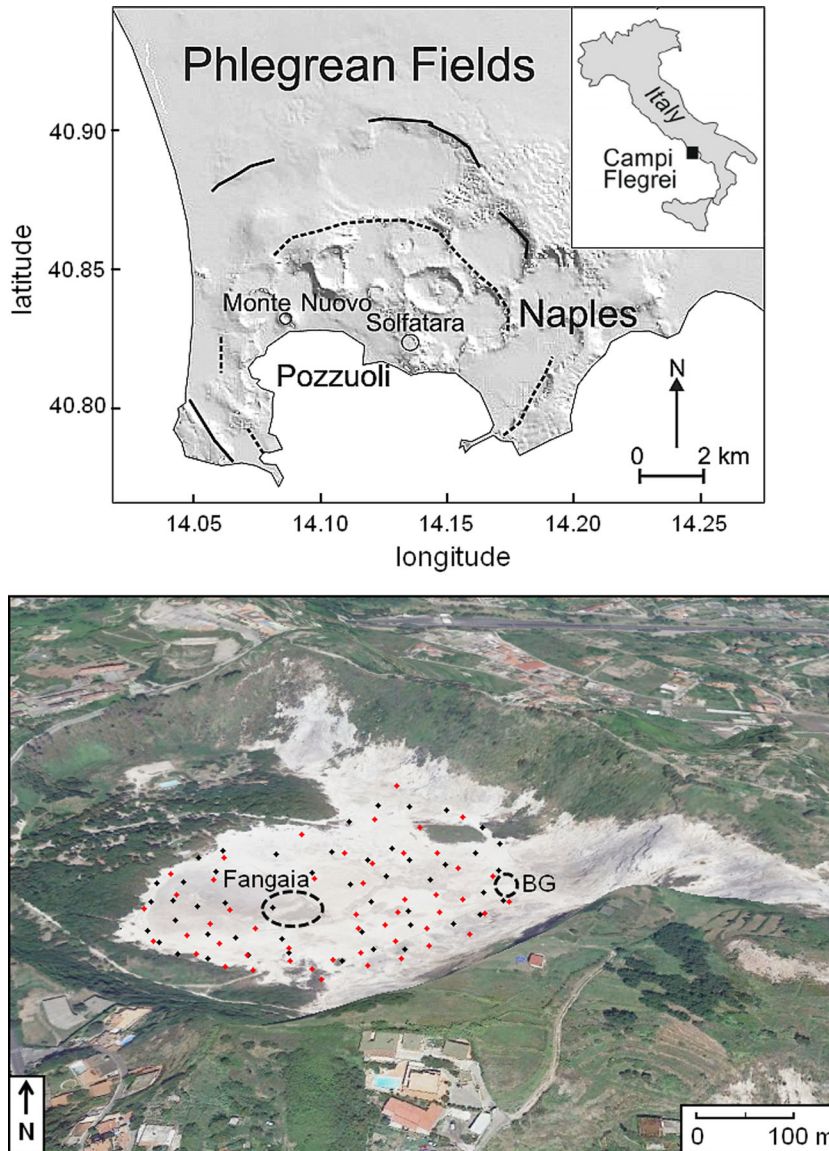


**Figure 4.** Top: structural sketch of the Solfatara volcano and surroundings. The lines indicate the borders of the two main calderas. Bottom: close-up view of the crater. The dots represent the installation sites of the seismic stations in 2014 May (black) and November (red). The dashed lines indicate the position of the Fangaia mud pool. BG (Bocca Grande) is the hottest fumarole of the Solfatara crater.

was divided into segments of 300 s, overlapping by 75 per cent, to reduce the variance in the PSD calculation (Cooley & Tukey 1965). The total power, representing the PSD estimate, was obtained from the square of the amplitude spectrum multiplied by the standard normalization factor  $2\Delta t = S$ , in which  $\Delta t$  is the sample interval and  $S$  is the number of samples (McNamara & Buland 2004).

For both recording periods at Solfatara, we observe very similar noise patterns with a predominant anthropogenic nature, as one can easily deduce from the time pattern of the PSDs (Fig. 5, Bianco *et al.* 2010). Between 4 Hz and approximately 10 Hz, the probability density functions are rather similar. For frequencies higher than 10 Hz, the large separation between the 5th and the 95th percentiles represents relatively large diurnal variations due to cultural activity but we cannot exclude any further hydrothermal influence (Bruno *et al.* 2007).

In order to quantify the strength of the signals, Fig. 6 shows an example of the resulting Green's function between two stations deployed in 2014 May at a distance of 177 m for a central fre-

quency of 5 Hz. For the ZZ and TT components, signals at positive and negative correlation lapse times are observed, corresponding to waves with almost similar energy propagating in opposite direction between the stations.

A clear difference in traveltime is observed between the waveforms on the TT and radial–radial (RR) correlations denoting Love and Rayleigh waves (dashed red lines in Fig. 6). Please note that, as described in Section 2, the exact traveltimes for each interstation pair to be used in the inversion procedure are calculated based on an interpolation between the weighted velocity values at the zero crossings of the Bessel function using the known distances between the sensors. Signal arrival times on the ZZ and the RR correlations are similar (clearly visible on the acausal part of the correlations), and result from Rayleigh waves. The TT correlation exhibits the slower Love wave arrival. Although both the ZZ and RR correlations contain the same Rayleigh wave signal, the ZZ correlations generally have higher SNR. In the following, for Rayleigh waves only the ZZ correlations will be used.

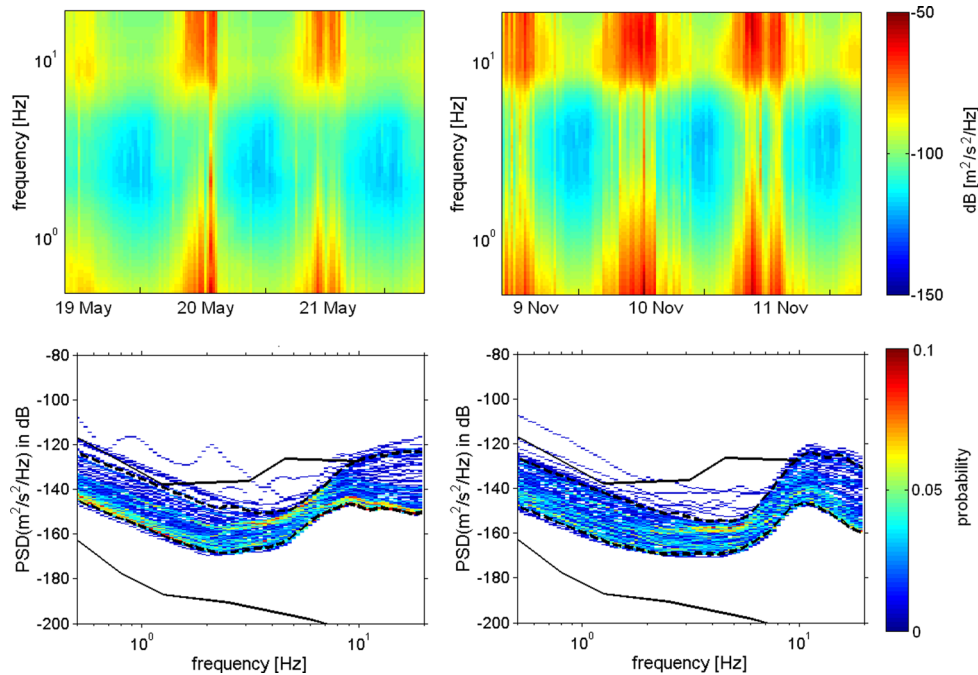


**Figure 5.** Top: PSDs in the frequency band 0.5–20 Hz for recording period in 2014 May (left) and November (right). Bottom: probability density function for 2014 May (left) and November (right). The Peterson model (Peterson 1993) is shown in black and the 5th and 95th percentiles of the distribution are shown as dashed black lines.

As can be seen in Fig. 6, the symmetry in the causal and acausal parts is not always fulfilled. As will be discussed later, this is most likely due to the distribution of noise sources and probably also due to local heterogeneities. As verified by frequency–wavenumber ( $f$ – $k$ ) analysis using the maximum likelihood method (Capon 1969) and by Petrosino *et al.* (2012), the distribution of noise sources—although not being uniform—guarantees a sufficient level of energy illuminating the wave propagation path between all sensors (e.g. Snieder 2004). Fig. 7 indicates that the distribution of the noise sources close to the lower and the upper end of the frequency band used is indeed different in the 2-D wavenumber plots. While at 4 Hz, the noise sources are distributed almost perfectly isotropically, at 13 Hz the sources are more scattered across the wavenumber plane, with the largest energy contribution coming from the eastern and southwestern directions. Although a non-uniform distribution of seismic noise sources might bias the reconstruction of the attenuation of the studied media, it will have only a very minor influence on the phase when taken over sufficiently long times (Shapiro & Campillo 2004), provided at least a minimum level of energy coming from the remaining azimuthal sectors.

### 6 3-D IMAGING OF THE SOLFATARA VOLCANO

Using ZZ and TT correlations and a fraction of two hours of the entire data set recorded on 2014 May 19, the inversion results after 500 iterations are shown in Fig. 8. The occurrence of strong lateral velocity variations is visible at first glance. The topmost layer is characterized by  $S$ -wave velocities ranging from 120 m s<sup>−1</sup> for the northeastern part of the crater up to 200 m s<sup>−1</sup> for the southwestern part. Such velocities values do largely agree with the findings of Serra *et al.* (2016). On the contrary, the lateral variations of the  $P$ -wave velocity are less pronounced. Immediately below the shallow deposits, an increase of the  $S$ -wave velocity starts in the southern

and central part at depths between 10 and 20 m (Fig. 8), probably at the lower boundary of the unconsolidated shallow deposits. The lower velocity area remains confined in the northern and southeastern part of the crater. At a depth of around 35 m, the  $S$ -wave velocity in the southern area increases up to 850 m s<sup>−1</sup>. At these depths, the volume seems to be divided in a higher velocity part (corresponding to the fumaroles area) and a lower one (corresponding to the northern edge), with a transition central zone. Below 40–45 m, the  $S$ -wave velocity increases up to 1100 m s<sup>−1</sup> in the southwestern area. Whereas the northeastern area is characterized by rather homogeneous  $S$ -wave velocities, there are clear spots of high  $P$ -wave velocities. The downmost slice (below 50 m) indicates that the high  $S$ -wave velocities extend towards the northeast similar to the  $P$ -wave velocities which reaches values up to 1900 m s<sup>−1</sup> and which, on the contrary, surround a low-velocity body in the centre of the crater. The absolute depth of the velocity contrasts and the corresponding calculated  $S$ -wave velocities are robust and compatible with the findings of previous studies (Petrosino *et al.* 2006, 2012).

### 7 SYNTHETIC TESTS

The pioneering works of geophysical inverse problems (e.g. Backus & Gilbert 1967, 1968, 1970) clearly recognized the importance of assessing solution robustness and the need to quantify inherent uncertainty. To ensure the reliability of the proposed technique, synthetic time-series of seismic noise were computed using the spectral element code GeoELSE, developed by the Center for Advanced Studies, Research and Development, in Sardinia, and the Department of Structural Engineering of the Politecnico di Milano (Faccioli *et al.* 1997).

For our test, the underlying physical model is largely representative of the natural example of the Solfatara crater (Fig. 9, top). For the  $P$ -wave velocity model (left column in Fig. 8), we also included some small-scale velocity variations. Since only

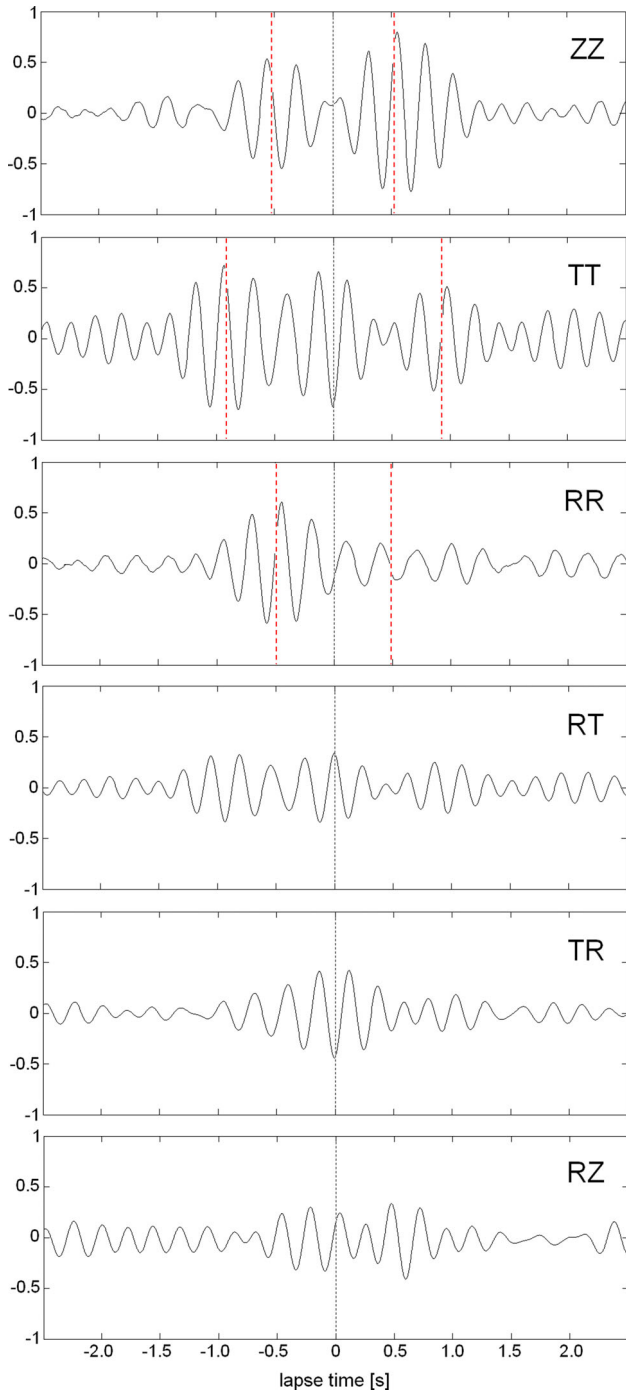


**Figure 6.** The bandpass filtered Green's function at central frequency of 5 Hz observed between two sensors at a distance of 177 m. Z, R and T denote vertical, radial and transverse, respectively. The dashed red lines represent the traveltimes between the sensors based on the interpolation between the velocity values at the zero crossings of the Bessel function (see the text for further details).

cultural noise higher than a few Hertz is considered, such synthetic wavefields can be modelled as a distribution of impulsive point forces located at the surface or subsurface of the studied medium, having random force orientation and amplitude (Lachet & Bard 1994). Such a random force was applied at each time step of 0.01 s at 200 different locations, arbitrarily distributed over an area covering

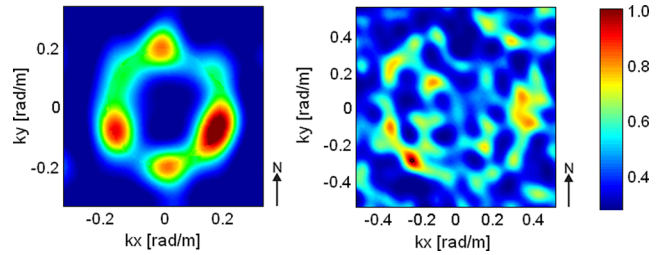


**Figure 7.**  $f$ - $k$  power density function showing the distribution of noise sources using the maximum likelihood method for 4 Hz (left) and 13 Hz (right).

the entire block's surface and a frame of 100 m width surrounding the block.

From the continuous data sets recorded by the same parametrization of the receivers, 60 noise windows of 30 s were extracted. As required by theory (Rawlinson & Spakman 2016), the same parametrization used for the real data inversion is used in the synthetic data inversion. Starting from a homogeneous 3-D velocity model, the entire inversion procedure is repeated five times for the same model realization using an identical parametrization to assess the uniqueness of the inverted velocity models.

As an example, Fig. 9 shows the inversion results for both the average  $P$ - and  $S$ -wave velocities for one run after 200 iterations. The comparison between the target structure and the calculated velocities shows that the structure is satisfactorily reproduced. The various layers characterized by different velocities are well separated and they can clearly be identified with sufficient resolution in depth. However, since a set of smoothing parameters has been introduced in the solution, no sharp velocity contrasts between the two blocks are found but there is only a more gradual transition. Moreover, as the resolution of our imaging technique is expected to decrease with depth, the tomographic signature of the velocity contrasts will become weaker with increasing depth.

Comparing the final results of various inversions based on the same parametrization, the variation in the results was found to be smaller than 5 per cent, meaning that the standard deviation is very small and the absolute velocity values are fairly well reproduced. Only a few isolated spots and the boundary area, for which the ray coverage was very sparse, have been found to show deviations up to 15 per cent. This means that once the correlation functions have been converged to stable values, robust and temporarily resolved velocity estimates can be obtained. Following Rawlinson & Spakman (2016), even in case of low SNRs, although small-scale elements might hardly be resolved, the main features and the temporarily more robust elements can still be recovered well by applying proper regularization parameters (i.e. smoothing and damping) in the inversion scheme.

## 8 NOISE-BASED 4-D MONITORING OF VELOCITY CHANGES

The last few years have seen clear signs of unrest at Solfatara, which have included ground deformation, earthquakes and variations in hydrothermal activity (Acocella *et al.* 2015; Chiodini *et al.* 2015). With the purpose of improving the temporal resolution for identifying and localizing changes in the shallow layers of the crater, we apply the inversion algorithm repeatedly to fractions of the entire data set. As in any monitoring technique, the time resolution, fixed by the time between two independent measurements, should be as small as possible. Fractions of two hours have been found to provide

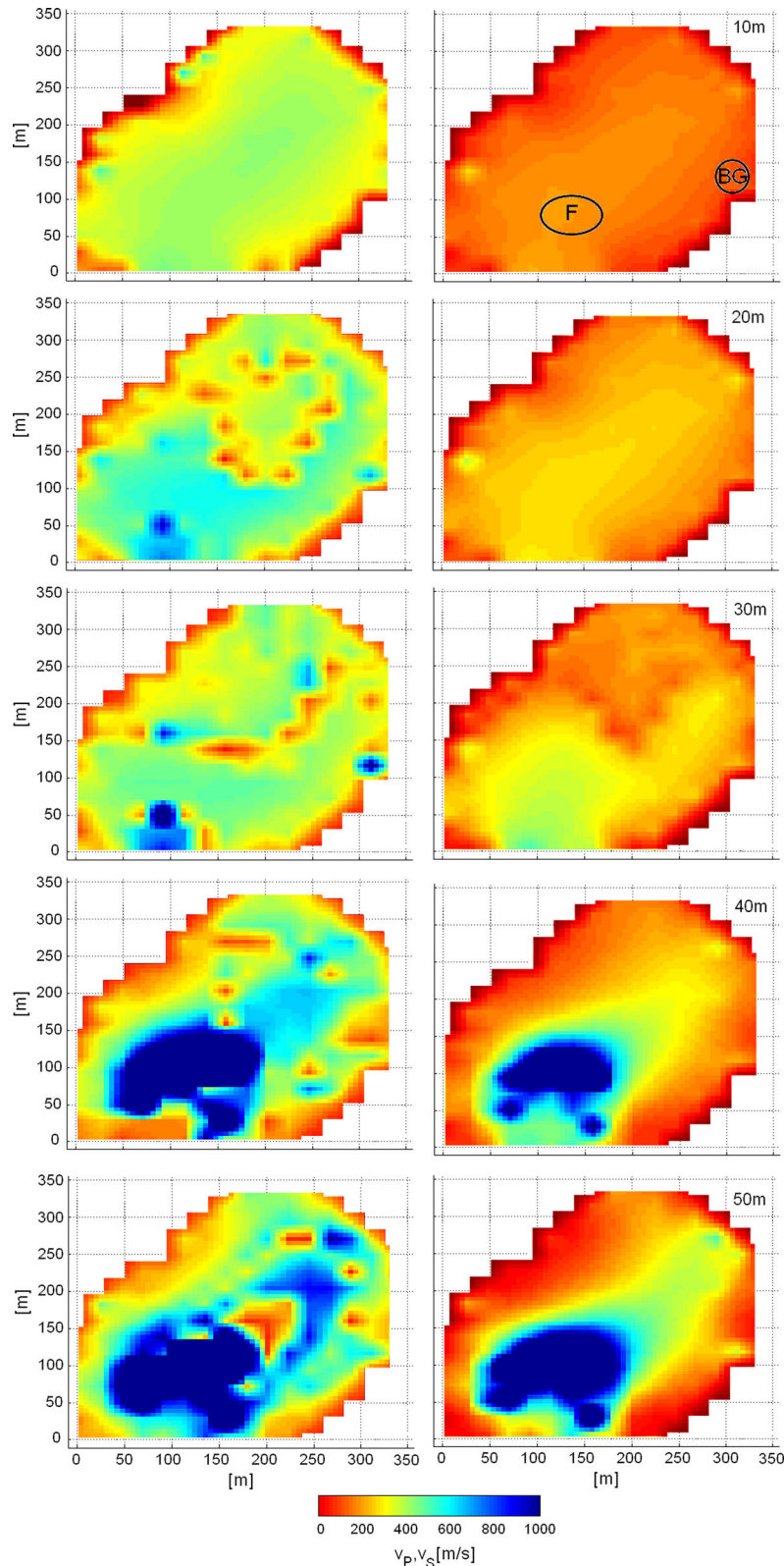


**Figure 8.** Horizontal cross-sections of the Solfatara volcano in terms of  $P$ -wave velocity (left) and  $S$ -wave velocity (right) and after inverting two hours of seismic noise on 2014 May 19. The positions of the Fangaia mud pool (F) and the Bocca Grande fumarole (BG) are indicated in the upper right plot.

stable velocity estimates, meaning that velocity variations within a few days can be monitored. Fig. 10 shows the relative velocity variations along the two installations between 2014 May 19 and 22 and between November 9 and 12 as well as the large ve-

locity variations between the two campaigns in 2014 May and November.

Although no unrest has been observed in the mentioned periods, velocity variations emerge even within a few days. This is particu-

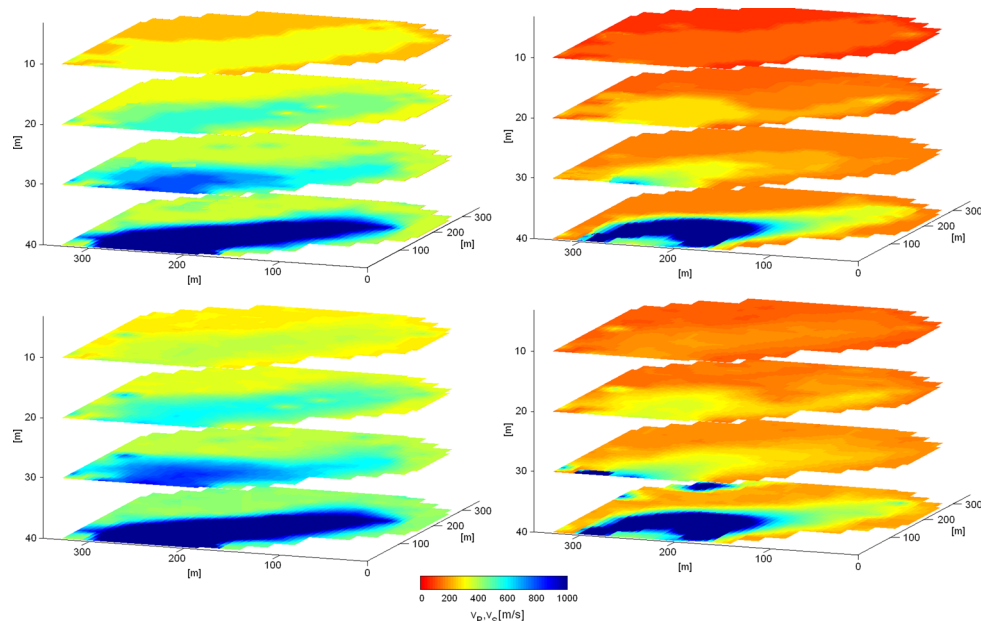


**Figure 9.** Top:  $P$ -wave velocity (left) and  $S$ -wave velocity (right) target models for validation test. Bottom: inversion results for  $P$ -wave velocity (left) and  $S$ -wave velocity (right). The images were obtained after 200 iterations.

larly obvious during the campaign in 2014 May. In 2014 November, only minor velocity variations are observed. As expected, the relative velocity variations within a few days are smaller compared to longer periods. However, the plots reveal that the shallow layers do not show any remarkable velocity variations whereas significant changes are present for deeper structures. In particular, between 2014 May and November, a marked decrease in velocity can be observed for the southwestern part of the crater whereas the velocity increases towards northeastward at depths lower than 30 m. For this area at the eastern edge of the Fangaia mud pool changes in velocity can also be observed between May 19 and 22. The depth range, for which the variations in velocity are depicted, coincides with the interface of gas-dominated reservoirs overlain by shallow conductive bodies interpreted as aquifers filled by condensate (e.g. Petrillo *et al.* 2013; Byrdina *et al.* 2014).

## 9 DISCUSSION

A better understanding of the structural framework of any caldera and its control on fluid and gas ascent are key requirements for a better definition of the role of any hydrothermal system during unrest (Acocella *et al.* 2015). To this regard, we need to define general patterns of the monitoring indicators and their possible relationships during unrest, with particular attention at identifying any general behaviour. The presented inversion algorithm based on seismic noise allows both the  $P$ - and  $S$ -wave velocities, which play a key role especially for lithology and fluid prediction methods, to be monitored with a high spatial and temporal resolution.

The relationships between the velocity structure and the inherent velocity changes are complex but some principal features can be recognized. The very shallow layers are characterized by only minor lateral velocity variations and the obtained  $S$ -wave velocities take standardized values of loose and unconsolidated pyroclastic deposits (Nunziata *et al.* 1999). For the northwestern sector of the studied area, close to the vegetation cover and associated background values of ground temperature and gas flux, the topmost

layers are characterized by rather low-velocity values. In this part of the crater non-saturated sands and tuffs can be found which are relatively undisturbed by the hydrothermal activity.

However, stratigraphy becomes more complex for deeper layers. For the eastern and northeastern sectors of the crater, an increase in velocity can be observed for depths larger than 30 m. The depth of the velocity contrast and the observed velocity values substantiate the hypothesis of the presence of a small volcanic edifice, likely a tuff-cone, formed during the phreatomagmatic activity in a smaller crater in the eastern sector (Petrosino *et al.* 2012). In turn, large lateral and vertical lithological and structural discontinuities in this part of the crater are mainly due to the superposition of the products related to this multievent activity.

The central Solfatarata area around the Fangaia mud pool, corresponding to lowest surface temperatures (Letort *et al.* 2012; Byrdina *et al.* 2014), is characterized by a significant velocity increase for depths larger than 25 m. In parallel, an increase of the  $v_p/v_s$  ratio can be found. This central zone can be interpreted as a mechanically soft and liquid-saturated part of the hydrothermal system, as compared to the drier and hotter zones in the eastern and northwestern sector of the study area. Although we did not consider the topographic relief in the inversion, it should be noted that this central zone has an elevation slightly lower than the surrounding area, and it usually drains the run-off waters from the southern part of the crater. High  $v_p/v_s$  ratios might indicate the existence of lithified bodies with a high density of saturated cracks (O'Connell & Budiansky 1974) and/or partial melt. Correspondingly, the lateral velocity variations at depths of more than 25 m (Fig. 8) delineate a distinct liquid-dominated conductive plume below the Fangaia mud pool. Such a highly conductive layer might be interpreted as an aquifer saturated with hot water condensing from a gas reservoir below (Byrdina *et al.* 2014). The aquifer is anomalously shallow for the water table height and the water temperature. However, such shallow water level might indicate that a pressurized gas plume sustains the aquifer here (Chiodini *et al.* 2015). In turn, the large-scale assumed cylindrical vertical velocity structure (Battaglia *et al.* 2008) might represent an easy way to transfer upflowing hydrothermal gases that cause the

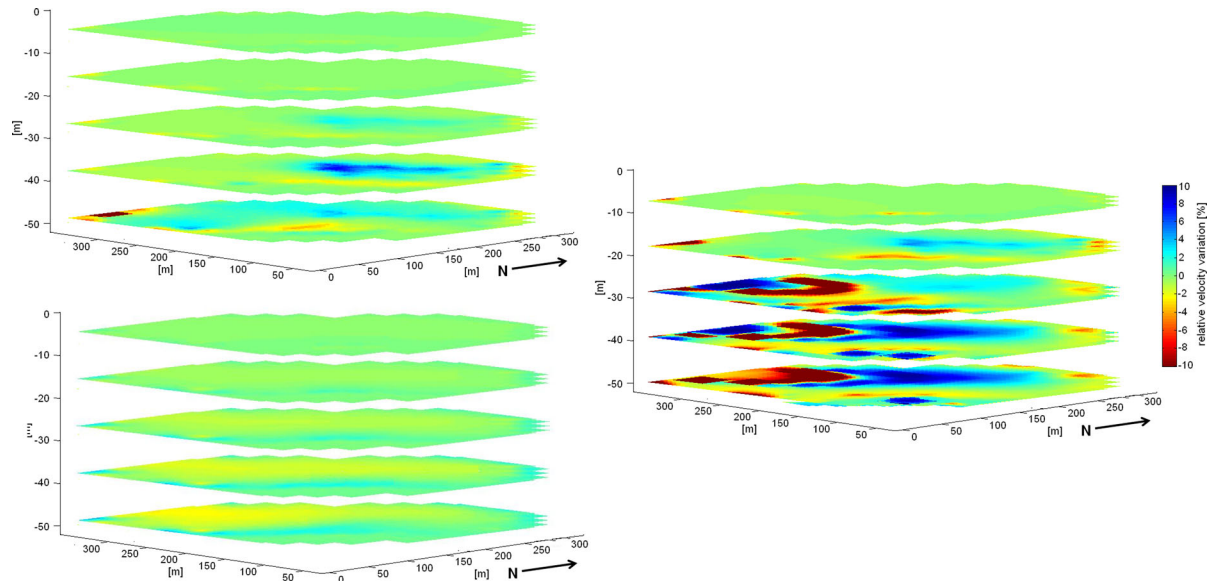


**Figure 10.** Relative  $S$ -wave velocity variations between 2014 May 19 and 22 with respect to 2014 May 19, 10:00 UTC (top-left), between 2014 November 9 and 12 with respect to 2014 November 9, 12:00 UTC (bottom-left) and between 2014 May and November with respect to 2014 May 22 (right).

evident surface anomalies in the gas flux, temperature and water-table level.

High-pressure values are also likely to influence the state of stress around the crater which, in turn, will influence the alignment of microcracks and pore space and therefore cause seismic anisotropy. In this case, a systematic azimuth-dependent (and nearly position independent) velocity shift might not be related to local heterogeneities. However, the traveltimes residuals after inversion as a function of azimuth (not shown) do not indicate any systematic bias with azimuth. This is in line with the interpretation of Petrosino *et al.* (2012) concluding that the polarization of seismic noise could be interpreted in terms of trapped surface waves affected by a high degree of heterogeneity characterizing the local lithology. The effect might hardly be caused by near-surface anisotropy. In the context of radial isotropy, a joint inversion of Love and Rayleigh waveforms is generally carried out for simultaneously calculating isotropic and radially anisotropic perturbations. As the presented algorithm does not aim at resolving radial anisotropy, we leave this issue for future studies.

On the other hand, smaller  $v_p/v_s$  ratios are found for the central part of the Solfatara crater at the eastern edge of the Fangaia mud pool towards the Fumarole sector. The comparison between the spatial variability of resistivity and gas flux emphasized a highly resistive body indicating that resistivity changes at this depth are related to high temperature gas saturation (Byrdina *et al.* 2014). Further evidence of a gas fluid reservoir comes from recent seismic attenuation imaging, recognizing a vertically extending, high attenuation structure (De Siena *et al.* 2010).

In turn, such a highly dynamic gas-dominated reservoir, which undergoes significant changes very quickly (Fig. 10), is probably driven by a long-term process of heating of the system. The heating, probably due to hot magmatic fluids entering the hydrothermal system (Chiodini *et al.* 2012) causes an evident increase in the hydrothermal activity very close to the surface. Based on physical simulations, Todesco (2009) could show that the increment in the flux of hot fluids would cause water vapour condensation within and at the border of the gas plume, and, in turn, heating of the rock by the latent heat release during condensation. Although the changes

at depth are in line with a high  $\text{CO}_2$  flux at the top (Byrdina *et al.* 2014), numerical simulations of gas transfer in hydrothermal system assess the physical feasibility of the delays between of changes at depth and the enlargement and the compositional variation of the fumaroles degassing processes at the surface (Chiodini *et al.* 2010, 2015), meaning that the structural variations at depth do not necessarily imply immediate changes at the surface. However, when taken over longer periods (i.e. between 2014 May and November, Fig. 10, right), the observed changes in the geochemical parameters occur simultaneously with the large and long-lasting changes in seismic velocity due to a sustained modification of the system.

## 10 CONCLUSIONS

Based on recordings of seismic noise at the Solfatara crater, we have shown that with a limited number of stations and recording times of several days, detailed images of the local  $P$ - and  $S$ -wave velocity structures as well as precise 3-D information on short-term changes therein can be obtained. The reliability of the proposed technique was validated using synthetic data sets showing that the results are well constrained. A combined use of Rayleigh and Love wave tomography can excel traditional methods in retrieving velocity heterogeneities at depth due to their different sensitivity kernels which allows the identification of large horizontal and vertical velocity variations and the spatially resolved mapping of  $P$ - and  $S$ -wave velocity contrasts. Such a precise knowledge of the velocity structure is particularly important at this volcano, where long-period seismic events associated to the activity of the hydrothermal system occur in the very shallow layers.

In a sort of continuous feedback process, hydrothermal and further geochemical and geophysical investigations of this area have been used to provide a correct interpretation of the spatial and temporal velocity changes. The lateral velocity variations delineate two plume structures: a liquid-dominated conductive plume for the southeastern part of the crater below the Fangaia mud pool and a gas-dominated plume in the central and western part of the Solfatara crater. Complementing traditional geoelectrical and geomagnetic field methods, we could show that seismic imaging can add an extra

dimension and a deeper perspective of the internal structure down to a depth of some tens of metres. Since the presented method only uses the phase and not the amplitude information associated with the direct or scattered waves, the scattered part of the correlation functions is stable enough to provide robust velocity estimates with a high temporal resolution. This allows not only static images of the velocity structure but also allow changes in the medium properties to be monitored and precisely localized with temporal resolution of two hours. Moreover, the development and the use of wireless sensor networks should ease the efforts necessary for the acquisition of seismic noise data, which will open the way to real-time 4-D imaging and monitoring of active volcanoes and possibly also seismic faults.

## ACKNOWLEDGEMENTS

Instruments were provided by the Geophysical Instrumental Pool of the GFZ Potsdam. We are grateful to Ralf Bauz from GFZ and students of Università degli studi di Napoli Federico II and the staff of Solfatara volcano who kindly allowed us to make measurements in excellent conditions. We are grateful to the editor Ana Ferreira and to two anonymous reviewers that contributed in improving the manuscript. The MED-SUV project has received funding from the European Union Seventh Framework Programme FP7 under grant agreement no. 308665.

## REFERENCES

- Acocella, V., Lorenzo, R. Di., Newhall, C. & Scandone, R., 2015. An overview of recent (1988 to 2014) caldera unrest: knowledge and perspectives, *Rev. Geophys.*, **53**, 896–955.
- Akamatsu, K., 1956a. Tomodás method for calculating the correlation coefficients as applied to microtremor analysis, *J. Phys. Earth*, **4**, 81–83.
- Akamatsu, K., 1956b. On microtremors, *Zisin (J. Seism. Soc. Japan)*, **2**, 21–40.
- Aki, K., 1957. Space and time spectra of stationary stochastic waves with special reference to microtremors, *Bull. Earthq. Res. Inst. Univ. Tokyo*, **35**, 415–456.
- Aki, K., 1965. A note on the use of microseisms in determining the shallow structures of the earth's crust, *Geophysics*, **30**, 665–666.
- Aki, K. & Richards, P., 1980. *Quantitative Seismic Theory and Methods*, W.H. Freeman.
- Arai, H. & Tokimatsu, K., 2004. S-wave velocity profiling by inversion of microtremor H/V spectrum, *Bull. seism. Soc. Am.*, **94**, 53–63.
- Backus, G. & Gilbert, F., 1967. Numerical applications of a formalism for geophysical inverse problems, *Geophys. J. Int.*, **13**, 247–276.
- Backus, G. & Gilbert, F., 1968. The resolving power of gross earth data, *Geophys. J. Int.*, **16**, 169–205.
- Backus, G. & Gilbert, F., 1970. Uniqueness in the inversion of inaccurate gross earth data, *Phil. Trans. R. Soc. Lond., A: Math. Phys. Eng. Sci.*, **266**, 123–192.
- Bartlett, M.S., 1948. Smoothing periodograms from time series with continuous spectra, *Nature*, **161**, 686–687.
- Battaglia, J., Zollo, A., Virieux, J. & Dello Iacono, D., 2008. Merging active and passive data sets in traveltimes tomography: the case study of Campi Flegrei caldera (Southern Italy), *Geophys. Prospect.*, **56**, 555–573.
- Bensen, G.D., Ritzwoller, M.H., Barmine, M.P., Levshin, A.L., Lin, F., Moschetti, M.P., Shapiro, N.M. & Yang, Y., 2007. Processing seismic ambient noise data to obtain reliable broad-band surface wave dispersion measurements, *Geophys. J. Int.*, **169**, 1239–1260.
- Bianco, F., Castellano, M., Cogliano, R., Cusano, P., Del Pezzo, E., Di Vito, M.A. & Petrosino, S., 2010. Caratterizzazione del noise sismico nell'area vulcanica dei Campi Flegrei: l'esperimento "UNREST", *Quad. Geofis.*, **86**, 1–19.
- Borchardt, R.D., 2008. *Viscoelastic Waves in Layered Media*, Cambridge Univ. Press.
- Boxberger, T., Picozzi, M. & Parolai, S., 2011. Shallow geology characterization using Rayleigh and Love wave dispersion curves derived from seismic noise array measurements, *J. appl. Geophys.*, **75**, 345–354.
- Bracewell, R.N., 1983. Discrete hartley transform, *J. Opt. Soc. Am.*, **73**, 1832–1835.
- Brenguier, F., Shapiro, N.M., Campillo, M., Nercessian, A. & Ferrazzini, V., 2007. 3-D surface wave tomography of the Piton de la Fournaise volcano using seismic noise correlations, *Geophys. Res. Lett.*, **34**, doi:10.1029/2006GL028586.
- Bruno, P.P.G., Ricciardi, G.P., Petrillo, Z., Di Fiore, V., Troiano, A. & Chiodini, G., 2007. Geophysical and hydrogeological experiments from a shallow hydrothermal system at Solfatara Volcano, Campi Flegrei, Italy: response to caldera unrest, *J. geophys. Res.*, **112**, doi:10.1029/2006JB004383.
- Bullen, K.E., 1963. An index of degree of chemical inhomogeneity in the Earth, *Geophys. J. Int.*, **7**, 584–592.
- Bullen, K.E. & Bolt, B.A., 1985. *An Introduction to the Theory of Seismology*, Cambridge Univ. Press.
- Byrdina, S. et al., 2014. Relations between electrical resistivity, carbon dioxide flux, and self-potential in the shallow hydrothermal system of Solfatara (Phlegrean Fields, Italy), *J. Volc. Geotherm. Res.*, **283**, 172–182.
- Campillo, M. & Paul, A., 2003. Long-range correlations in the diffuse seismic coda, *Science*, **299**, 547–549.
- Capon, J., 1969. High-resolution frequency-wavenumber spectrum analysis, *Proc. IEEE*, **57**, 1408–1418.
- Capon, J., Greenfield, R.J. & Kolker, R.J., 1967. Multidimensional maximum-likelihood processing of a large aperture seismic array, *Proc. IEEE*, **55**, 192–211.
- Chávez-García, F.J. & Luzón, F., 2005. On the correlation of seismic microtremors, *J. geophys. Res.*, **110**, doi:10.1029/2005JB003671.
- Chiodini, G., Avino, R., Caliro, S. & Minopoli, C., 2011. Temperature and pressure gas geoindicators at the Solfatara fumaroles (Campi Flegrei), *Ann. Geophys.*, **54**, 151–160.
- Chiodini, G., Caliro, S., Cardellini, C., Granieri, D., Avino, R., Baldini, A., Donnini, M. & Minopoli, C., 2010. Long-term variations of the Campi Flegrei, Italy, volcanic system as revealed by the monitoring of hydrothermal activity, *J. geophys. Res.*, **115**(B3), B03205, doi:10.1029/2008JB006258.
- Chiodini, G., Caliro, S., De Martino, P., Avino, R. & Gherardi, F., 2012. Early signals of new volcanic unrest at Campi Flegrei caldera? Insights from geochemical data and physical simulations, *Geology*, **40**(10), 943–946.
- Chiodini, G., Vandemeulebrouck, J., Caliro, S., D'Auria, L., De Martino, P., Mangiacapra, A. & Petrillo, Z., 2015. Evidence of thermal-driven processes triggering the 2005–2014 unrest at Campi Flegrei caldera, *Earth planet. Sci. Lett.*, **414**, 58–67.
- Cho, K.H., Herrmann, R.B., Ammon, C.J. & Lee, K., 2007. Imaging the upper crust of the Korean Peninsula by surface-wave tomography, *Bull. seism. Soc. Am.*, **97**, 198–207.
- Chouet, B., De Luca, G., Milana, G., Dawson, P., Martini, M. & Scarpa, R., 1998. Shallow velocity structure of Stromboli volcano, Italy, derived from small-aperture array measurements of Strombolian tremor, *Bull. seism. Soc. Am.*, **88**, 653–666.
- Claerbout, J.F., 1968. Synthesis of a layered medium from its acoustic transmission response, *Geophysics*, **33**, 264–269.
- Cooley, J.W. & Tukey, J.W., 1965. An algorithm for the machine calculation of complex Fourier series, *Math. Comput.*, **19**, 297–301.
- de Ridder, S. & Dellinger, J., 2011. Ambient seismic noise eikonal tomography for near-surface imaging at Valhall, *Leading Edge*, **30**, 506–512.
- de Siena, L., Del Pezzo, E. & Bianco, F., 2010. Seismic attenuation imaging of Campi Flegrei: evidence of gas reservoirs, hydrothermal basins, and feeding systems, *J. geophys. Res.*, **115**, doi:10.1029/2009JB006938.
- Ekström, G., Abers, G.A. & Webb, S.C., 2009. Determination of surface-wave phase velocities across USArray from noise and Aki's spectral formulation, *Geophys. Res. Lett.*, **36**, doi:10.1029/2009GL013911.

- Faccioli, E., Maggio, F., Paolucci, R. & Quarteroni, A., 1997. 2D and 3D elastic wave propagation by a pseudo-spectral domain decomposition method, *J. Seismol.*, **1**, 237–251.
- Golub, G.H. & Reinsch, C., 1970. Singular value decomposition and least squares solutions, *Numer. Math.*, **14**, 403–420.
- Granieri, D., Avino, R. & Chiodini, G., 2010. Carbon dioxide diffuse emission from the soil: ten years of observations at Vesuvio and Campi Flegrei (Pozzuoli), and linkages with volcanic activity, *Bull. Volcanol.*, **72**, 103–118.
- Grêt, A., Snieder, R., Aster, R.C. & Kyle, P.R., 2005. Monitoring rapid temporal change in a volcano with coda wave interferometry, *Geophys. Res. Lett.*, **32**, doi:10.1029/2004GL021143.
- Henstridge, J.D., 1979. A signal processing method for circular arrays, *Geophysics*, **44**, 179–184.
- Horiike, M., 1985. Inversion of phase velocity of long-period microtremors to the S-wave-velocity structure down to the basement in urbanized areas, *J. Phys. Earth*, **33**, 59–96.
- Kimman, W.P. & Trampert, J., 2010. Approximations in seismic interferometry and their effects on surface waves, *Geophys. J. Int.*, **182**, 461–476.
- Kissling, E., 1988. Geotomography with local earthquake data, *Rev. Geophys.*, **25**, 659–698.
- Köhler, A., Ohrnberger, M., Scherbaum, F., Wathelet, M. & Cornou, C., 2007. Assessing the reliability of the modified three-component spatial autocorrelation technique, *Geophys. J. Int.*, **168**, 779–796.
- Lachet, C. & Bard, P.Y., 1994. Numerical and theoretical investigations on the possibilities and limitations of Nakamura's technique, *J. Phys. Earth*, **42**, 377–397.
- Larose, E., Roux, P., Campillo, M. & Derode, A., 2008. Fluctuations of correlations and Green's function reconstruction: role of scattering, *J. appl. Phys.*, **103**, 114907, doi:10.1063/1.2939267.
- Lay, T. & Wallace, T.C., 1995. *Modern Global Seismology*, Academic Press.
- Lee, W.B. & Solomon, S.C., 1979. Simultaneous inversion of surface-wave phase velocity and attenuation: Rayleigh and Love waves over continental and oceanic paths, *Bull. seism. Soc. Am.*, **69**, 65–95.
- Letort, J., Roux, P., Vandemeulebrouck, J., Coutant, O., Cros, E., Wathelet, M., Cardellini, C. & Avino, R., 2012. High-resolution shallow seismic tomography of a hydrothermal area: application to the Solfatara, Pozzuoli, *Geophys. J. Int.*, **189**, 1725–1733.
- Lin, F.C., Moschetti, M.P. & Ritzwoller, M.H., 2008. Surface wave tomography of the western United States from ambient seismic noise: Rayleigh and Love wave phase velocity maps, *Geophys. J. Int.*, **173**, 281–298.
- Long, T.L., 2000. Seismic surface-wave tomography of waste sites, Report DOE/ER/14706, Georgia Inst. of Tech., Atlanta, US.
- Long, L.T. & Kocaoglu, A.H., 2001. Surface-wave group-velocity tomography for shallow structures, *J. Environ. Eng. Geophys.*, **6**, 71–81.
- Madonia, P., Federico, C., Cusano, P., Petrosino, S., Aiuppa, A. & Gurrieri, S., 2008. Crustal dynamics of Mount Vesuvius from 1998 to 2005: effects on seismicity and fluid circulation, *J. geophys. Res.*, **113**, doi:10.1029/2007JB005210.
- Malagnini, L., Rovelli, A., Hough, S.E. & Seeber, L., 1993. Site amplification estimates in the Garigliano Valley, Central Italy, based on dense array measurements of ambient noise, *Bull. seism. Soc. Am.*, **83**, 1744–1755.
- Marquardt, D.W., 1963. An algorithm for least squares estimation of non-linear parameters, *J. Soc. Indust. Appl. Math.*, **2**, 431–441.
- McMechan, G.A. & Yedlin, M.J., 1981. Analysis of dispersive waves by wave field transformation, *Geophysics*, **46**, 869–874.
- McNamara, D.E. & Buland, R.P., 2004. Ambient noise levels in the continental United States, *Bull. seism. Soc. Am.*, **94**, 1517–1527.
- Menke, W. & Jin, G., 2015. Waveform fitting of cross spectra to determine phase velocity using Aki's formula, *Bull. seism. Soc. Am.*, **105**, 1619–1627.
- Métaxian, J.P., Lesage, P. & Dorel, J., 1997. Permanent tremor of Masaya Volcano, Nicaragua: wave field analysis and source location, *J. geophys. Res.*, **102**, 22 529–22 545.
- Miller, D.S. & Smith, R.B., 1999. P and S velocity structure of the Yellowstone volcanic field from local earthquake and controlled-source tomography, *J. geophys. Res.*, **104**, 15 105–15 121.
- Miller, R.D., Xia, J., Park, C.B. & Ivanov, J.M., 1999. Multichannel analysis of surface waves to map bedrock, *Leading Edge*, **18**, 1392–1396.
- Mordret, A., Landès, M., Shapiro, N.M., Singh, S.C., Roux, P. & Barkved, O.I., 2013. Near-surface study at the Valhall oil field from ambient noise surface wave tomography, *Geophys. J. Int.*, **193**, 1627–1643.
- Moschetti, M.P., Ritzwoller, M.H., Lin, F.C. & Yang, Y., 2010. Crustal shear wave velocity structure of the western United States inferred from ambient seismic noise and earthquake data, *J. geophys. Res.*, **115**, doi:10.1029/2010JB007448.
- Nakata, N., Boué, P., Brenguier, F., Roux, P., Ferrazzini, V. & Campillo, M., 2016. Body-and surface-wave reconstruction from seismic-noise correlations between arrays at Piton de la Fournaise volcano, *Geophys. Res. Lett.*, **43**, 1047–1054.
- Nunziata, C., Mele, R. & Natale, M., 1999. Shear-wave velocities and primary influencing factors of Campi Flegrei–Neapolitan deposits, *Eng. Geol.*, **54**, 299–312.
- O'Connell, R.J. & Budiansky, B., 1974. Seismic velocities in dry and saturated cracked solids, *J. geophys. Res.*, **79**, 5412–5426.
- Othori, M., Nobata, A. & Wakamatsu, K., 2002. A comparison of ESAC and FK methods of estimating phase velocity using arbitrarily shaped microtremor arrays, *Bull. seism. Soc. Am.*, **92**, 2323–2332.
- Okada, H., 2003. *The Microtremor Survey Method*, Vol. **12**, Society of Exploration Geophysicists, Tulsa, USA.
- Park, C.B., Miller, R.D. & Xia, J., 1999. Multichannel analysis of surface waves, *Geophysics*, **64**, 800–808.
- Parolai, S., Richwalski, S.M., Milkereit, C. & Fäh, D., 2006. S-wave velocity profiles for earthquake engineering purposes for the Cologne area (Germany), *Bull. Earthq. Engin.*, **4**(1), 65–94.
- Peterson, J., 1993. Observations and modeling of seismic background noise, U.S. Geol. Surv. Open File Rep., 93-322.
- Petrillo, Z., Chiodini, G., Mangiacapra, A., Caliro, S., Capuano, P., Russo, G., Cardellini, C. & Avino, R., 2013. Defining a 3D physical model for the hydrothermal circulation at Campi Flegrei caldera (Italy), *J. Volc. Geotherm. Res.*, **264**, 172–182.
- Petrosino, S., Cusano, P. & Saccorotti, G., 2006. Shallow shear-wave velocity structure of Solfatara volcano (Campi Flegrei, Italy), from inversion of Rayleigh-wave dispersion curves, *Boll. Geofis. Teor. Appl.*, **47**, 89–103.
- Petrosino, S., Damiano, N., Cusano, P., Di Vito, M.A., Vita, S. & Del Pezzo, E., 2012. Subsurface structure of the Solfatara volcano (Campi Flegrei caldera, Italy) as deduced from joint seismic-noise array, volcanological and morphostructural analysis, *Geochem. Geophys. Geosyst.*, **13**, doi:10.1029/2011GC004030.
- Picozzi, M., Parolai, S., Bindi, D. & Strollo, A., 2009. Characterization of shallow geology by high-frequency seismic noise tomography, *Geophys. J. Int.*, **176**, 164–174.
- Pilz, M., Parolai, S. & Bindi, D., 2013. Three-dimensional passive imaging of complex seismic fault systems: evidence of surface traces of the Issyk-Ata fault (Kyrgyzstan), *Geophys. J. Int.*, **194**, 1955–1965.
- Pilz, M., Parolai, S., Bindi, D., Saponaro, A. & Abdybachev, U., 2014. Combining seismic noise techniques for landslide characterization, *Pure appl. Geophys.*, **171**, 1729–1745.
- Pilz, M., Parolai, S., Picozzi, M. & Bindi, D., 2012. Three-dimensional shear wave velocity imaging by ambient seismic noise tomography, *Geophys. J. Int.*, **189**, 501–512.
- Ratdomopurbo, A. & Poupinet, G., 1995. Monitoring a temporal change of seismic velocity in a volcano: application to the 1992 eruption of Mt. Merapi (Indonesia), *Geophys. Res. Lett.*, **22**, 775–778.
- Rawlinson, N. & Spakman, W., 2016. On the use of sensitivity tests in seismic tomography, *Geophys. J. Int.*, **205**, 1221–1243.
- Renalier, F., Jongmans, D., Campillo, M. & Bard, P.Y., 2010. Shear wave velocity imaging of the Avignonet landslide (France) using ambient noise cross correlation, *J. geophys. Res.*, **115**, doi:10.1029/2009JF001538.
- Sabra, K.G., Gerstoft, P., Roux, P., Kuperman, W.A. & Fehler, M.C., 2005. Extracting time-domain Green's function estimates from ambient seismic noise, *Geophys. Res. Lett.*, **32**, doi:10.1029/2004GL021862.
- Saccorotti, G., Chouet, B. & Dawson, P., 2003. Shallow-velocity models at the Kilauea Volcano, Hawaii, determined from array analyses of tremor wavefields, *Geophys. J. Int.*, **152**, 633–648.

- Serra, M., Festa, G., Roux, P., Gresse, M., Vandemeulebrouck, J. & Zollo, A., 2016. A strongly heterogeneous hydrothermal area imaged by surface waves: the case of Solfatara, Campi Flegrei, Italy, *Geophys. J. Int.*, **205**, 1813–1822.
- Shapiro, N.M. & Campillo, M., 2004. Emergence of broadband Rayleigh waves from correlations of the ambient seismic noise, *Geophys. Res. Lett.*, **31**, doi:10.1029/2004GL019491.
- Shapiro, N.M., Campillo, M., Stehly, L. & Ritzwoller, M.H., 2005. High-resolution surface-wave tomography from ambient seismic noise, *Science*, **307**, 1615–1618.
- Snieder, R., 2004. Extracting the Green's function from the correlation of coda waves: a derivation based on stationary phase, *Phys. Rev. E*, **69**, 046610, doi:10.1103/PhysRevE.69.046610.
- Stehly, L., Campillo, M. & Shapiro, N.M., 2006. A study of the seismic noise from its long-range correlation properties, *J. geophys. Res.*, **111**, doi:10.1029/2005JB004237.
- Strollo, A., Parolai, S., Jäckel, K.H., Marzorati, S. & Bindi, D., 2008. Suitability of short-period sensors for retrieving reliable H/V peaks for frequencies less than 1 Hz, *Bull. seism. Soc. Am.*, **98**, 671–681.
- Tang, X.M., Li, C. & Patterson, D.J., 2010. A curve-fitting technique for determining dispersion characteristics of guided elastic waves, *Geophysics*, **75**, 153–160.
- Tarantola, A., 1987. *Inverse Problem Theory*, Elsevier Science Publications.
- Todesco, M., 2009. Signals from the Campi Flegrei hydrothermal system: role of a magmatic source of fluids, *J. geophys. Res.*, **114**, B05201, doi:10.1029/2008JB006134.
- Tokimatsu, K., 1997. Geotechnical site characterization using surface waves, in *Proceedings of 1st Conference on Earthquake Geotechnical Engineering*, Vol. 3, pp. 1333–1368, ed. Ishihara, K. & Balkema, A.A.
- Tukey, J.W., 1974. Introduction to today's data analysis, in *Proceedings of Conference on Critical Evaluation of Chemical and Physical Structural Information*, pp. 3–14, National Academy of Sciences, Washington.
- Vilardo, G., Sansivero, F. & Chiodini, G., 2015. Long-term TIR imagery processing for spatiotemporal monitoring of surface thermal features in volcanic environment: a case study in the Campi Flegrei (Southern Italy), *J. geophys. Res.*, **120**, 812–826.
- Weaver, R.L. & Lobkis, O.I., 2001. Ultrasonics without a source: thermal fluctuation correlations at MHz frequencies, *Phys. Rev. Lett.*, **87**, 134301, doi:10.1103/PhysRevLett.87.134301.
- Wegler, U., Lühr, B.G., Snieder, R. & Ratdomopurbo, A., 2006. Increase of shear wave velocity before the 1998 eruption of Merapi volcano (Indonesia), *Geophys. Res. Lett.*, **33**, doi:10.1029/2006GL025928.
- Yang, Y., Ritzwoller, M.H., Levshin, A.L. & Shapiro, N.M., 2007. Ambient noise Rayleigh wave tomography across Europe, *Geophys. J. Int.*, **168**, 259–274.
- Yanovskaya, T.B. & Ditmar, P.G., 1990. Smoothness criteria in surface wave tomography, *Geophys. J. Int.*, **102**, 63–72.
- Yao, H., Beghein, C. & van der Hilst, R.D., 2008. Surface wave array tomography in SE Tibet from ambient seismic noise and two-station analysis-II. Crustal and upper-mantle structure, *Geophys. J. Int.*, **173**, 205–219.
- Yao, H., van der Hilst, R.D. & Maarten, V., 2006. Surface-wave array tomography in SE Tibet from ambient seismic noise and two-station analysis—I. Phase velocity maps, *Geophys. J. Int.*, **166**, 732–744.